Turbulence transition in stratified atmospheric and oceanic shear flows: Reynolds and Prandtl number controls upon the mechanism

A. Mashayek[1] and W. R. Peltier[1]

[1] We provide detailed analyses of the role of secondary instabilities in the transition to turbulence of stratified shear flows at the high Reynolds and Prandtl numbers appropriate to the atmosphere and ocean. Our focus is upon a series of recent observations suggestive of a marked change in the mechanism of transition in this laboratory inaccessible regime. Our results demonstrate the joint dependance of the transition mechanism on these two nondimensional parameters. We discuss the primary transition mechanisms of shear aligned convective instability, stagnation point instability and shear instabilities of the braid in detail. **Citation:** Mashayek, A., and W. R. Peltier (2011), Turbulence transition in stratified atmospheric and oceanic shear flows: Reynolds and Prandtl number controls upon the mechanism, *Geophys. Res. Lett.*, *38*, L16612, doi:10.1029/2011GL048542.

1. Introduction

[2] Stratified parallel free shear flows are known to be susceptible to a range of primary instabilities, the most common of which is the Kelvin-Helmholtz (KH) instability. This is generally of a two-dimensional (2D) form but the finite amplitude KH billows so-produced are prone to a range of secondary instabilities that facilitate the transition to fully developed three-dimensional (3D) turbulence. The secondary instabilities include the pairing instability and the secondary convective instability (SCI) [*Klaassen and Peltier*, 1985, hereinafter KP85; *Caulfield and Peltier*, 2000, hereinafter CP00; *Peltier and Caulfield*, 2003]. Increasingly relevant in the recent literature is the secondary shear instability (SSI) of the vorticity braid that forms between adjacent billow cores [*Corcos and Sherman*, 1976], a mode that has received recent attention from *Staquet* [2000] and *Smyth* [2004]. Experimental analyses of the range of secondary structures that develop in laboratory shear flows have been reviewed by *Thorpe* [2005] and observations of them in the oceanic environment have been described by *Bourgault et al.* [2001], *Moum et al.* [2003], *van Haren and Gostiaux* [2010] and *Geyer et al.* [2010, hereinafter G10]. Atmospheric examples are also ubiquitous and have been described by *Gossard* [1990] and *Luce et al.* [2010].

[3] Of special interest is the mechanism or mechanisms that govern turbulent collapse of the primary 2D KH structure. Although both atmosphere and ocean are characterized by high Reynolds numbers, they are distinguished by a marked difference in the Prandtl number which is approximately unity in the atmosphere but in the oceanic thermocline may be in the range 7–9 or in an estuarine shear zone on the order of hundreds. Our interest in this paper is in the joint dependence of the transition mechanism upon these two non-dimensional parameters.

[4] Various 2D numerical simulations [*Staquet*, 1995; *Smyth*, 2004] have been employed to study the role of SSI in transition to turbulence and the recent observationally motivated study of G10 has advocated the view that such braid shear instability is the main mechanism responsible for transition at high Reynolds numbers. Herein we make the case that none of these analyses were capable of ruling out the important role of the 3D SCI mechanism as the analyses were based on 2D simulations and therefore explicitly eliminated the possibility of SCI. Our argument is based on recent theoretical studies [*Mashayek and Peltier*, 2011, hereinafter MP1] which suggest that while SSI may be a prominent instability growing on the braid (especially in the early stages of KH wave evolution), at high Reynolds numbers SCI remains the dominant player in the transition process. This mode is originally focused within the super-adiabatic regions (SAR's) that develop within the cores. In this study we address the question as to whether this continues to hold true as the Prandtl number increases. We will show that the emergence and interactions of various secondary modes are governed by the combined influence of the Reynolds and Prandtl numbers as well as the stratification. We will also show that for a flow to be influenced by SSI vortices on the braid, the Reynolds numbers need not be as high as suggested by G10 and that a scenario in which SSI is prominent also arises at much lower Reynolds numbers (of order 10000) provided that the Prandtl number is sufficiently low. We also further investigate the role of the recently-discovered Stagnation Point Instability (SPI) (MP1) as a contributor to the transition mechanism. It seems to us that this instability may already have been captured in the observations but not identified as such.

2. Non-separable Stability Analysis

[5] We begin by considering the evolution of a stratified shear layer with initial background profiles of $U(z) = U_0 \tanh(z/h)$ and $\rho(z) = \rho_a - \rho_0 \tanh(Rz/h)$ where U_0 and ρ_0 are reference velocity and density, h is half of the shear layer thickness, and R is the ratio of the characteristic scale of velocity variation to that of the density variation and is chosen to be 1.1 based on conventional laboratory experiments in which the working fluid consists of salt stratified water. The Reynolds number is defined by $Re = U_0 h/\nu$ where ν is the kinematic viscosity and the Prandtl number by $Pr = \nu/\kappa$

[1]Department of Physics, University of Toronto, Toronto, Ontario, Canada.

where κ is the thermal diffusivity. Note that our definition of Re leads to numbers four times smaller than those defined based on velocity difference across the shear layer ($2U_0$) and full thickness of the layer ($2h$) which is often used in the experimental literature. The stratification at the center of the shear layer is measured by the gradient Richardson number $Ri(z) = N^2/(dU/dz)^2$ where N is the buoyancy frequency. We start by performing non-separable linear stability analyses similar to those of KP85 but at much higher Reynolds number. Details of the analyses can be found in the auxiliary material.[1] MP1 performed such analyses on a periodic train of KH billows for a case with $Re = 1000$, $Pr = 1$ and $Ri = 0.12$. Here we repeat the analysis for a higher Reynolds number of 2000. Figure 1 presents the results of the analyses applied to two wavelengths of the fastest growing mode (FGM) of KH instability to allow for pairing interaction. Figure 1b shows the Perturbation Kinetic Energy (PKE) eigenfunction for the pairing instability. This mode is found to be of a 3D nature with small spanwise wavenumbers. Figure 1c illustrates the PKE eigenfunction of the SCI. The FGM of this mode has a spanwise wavenumber of ~10. Figure 1d illustrates the eigenfunction for the SSI which is also of a 3D nature. Figure 1e shows an instability discovered by MP1 which is localized to the braid stagnation point and which we refer to as the Stagnation Point Instability (SPI). SPI is also of an inherently 3D nature with a spanwise wavenumber close to that of the SCI. Figure 1f shows the eigenfunction of an instability referred to as the Localized Core Vortex Instability (LCVI) which is localized to the vorticity bands with negative vorticity (i.e., opposed to the direction of the original shear layer's vorticity) inside the cores. Figure 1g shows the eigenfunction of another 3D mode called the Secondary Vorticity Band Instability (SVBI) which emerges due to the effect of the velocity field induced by the vorticity bands inside the cores on the strain field associated with the braid (MP1). It should be noted that SVBI is similar to SPI in the sense that it tends to twist the braid at the stagnation point. Moreover, both modes are excited due to interaction between the core vorticity bands and the braid strain field. Therefore, they can be considered to be members of one family. However, it should be noted that SVBI induces deformation at the corners of the cores while SPI is more local to the braid stagnation point. In Figures 1f and 1g, the eigenfunctions are overlain on the vorticity contours to help with visualization of the location of the secondary instabilities (shown in Figures 1a–1e) with respect to the primary KH wave. Figure 1a describes the time evolution of the growth rates of each of the secondary instabilities over the course of flow evolution. The first vertical dashed line corresponds to the time at which the KH billow reaches its maximum amplitude and the second vertical dashed line corresponds to the onset of the pairing instability in the 2D simulations which provide the background 2D flow for our stability analysis.

[6] MP1 investigated the interaction between SPI, SSI, SCI and pairing modes at $Pr = 1$ and over a range of Reynolds and Richardson numbers. In this study we focus on the combined influence of the Prandtl and Reynolds numbers on the evolution of secondary instabilities. We will

show that apart from the SSI and SCI, SPI and SVBI may also play important roles in the transition to turbulence.

3. Joint Influence of *Re*, *Pr* and *Ri*

[7] MP1 employed an heuristic model as a means of helping to understand on *a priori* grounds the dependence of the possibility of occurrence of the SSI and the SCI on the values of *Pr*, *Re* and *Ri* (see auxiliary material for more details). We showed that an increase in *Pr* enhances the possibility of SCI emergence (at fixed *Re* and *Ri*) and that at a higher *Pr*, the SCI is more likely to occur at lower Reynolds numbers.

[8] Furthermore, it was shown by MP1 that an increase in the Reynolds number promotes the SSI (consistent with previous studies of *Smyth* [2004] and *Staquet* [1995]). Also, an increase in the Prandtl number shifts the SSI-unstable region to higher Reynolds numbers meaning that even though an increase in *Re* leads to increase in the importance of secondary instability on the braid, increase in *Pr* tends to act in the opposite direction and suppress braid instabilities. Therefore, to observe braid instabilities at high Prandtl numbers in the salt stratified ocean one needs to be at sufficiently high Reynolds numbers (such as in the observations reported by G10). This implies that the emergence of braid instability (such as suggested by G10) can be observed at much lower Reynolds numbers than suggested by G10 provided that the Prandtl number is sufficiently low. Therefore, salt-stratified laboratory experiments are unlikely candidates for detection of this scenario (due to very large *Pr*) but atmospheric KH-waves are suitable for observing a great deal of braid activity at Reynolds numbers even as low as ~10^4.

[9] Additionally, the heuristic mode of MP1 suggests that increase in either *Pr* or *Re* enhances the possibility of occurrence of SCI. Therefore, the claim of G10 that SSI must be the main instability responsible for transition to turbulence at high *Re* is subject to three important caveats: First, the SCI is likely to remain a dominant player in the transition process together with the SSI; second, SPI may play a critical role in the transition process. If so, how is its role influenced by variations in *Pr* and *Ri*?; third, is it possible to observe SSI playing an important role at Reynolds numbers much lower than proposed by G10 provided that *Pr* is small enough? In the remainder of this paper we address these questions.

4. Computational Results and Discussion

[10] We proceed first to investigate the finite amplitude growth rates of the instabilities described in the previous sections by employing Direct Numerical Simulation (DNS) performed at various values of *Re*, *Pr* and *Ri*. More information on the details of the simulations and the choice of the domain length scale can be found in the auxiliary material. Figure 2 shows spanwise and streamwise vorticity iso-surfaces for four cases with various Reynolds numbers but all at $Pr = 1$ and $Ri = 0.12$. The spanwise vorticity isosurfaces (green) show that SSI emerges in the braid for $Re > 4000$ with both the number and wavenumber of SSI vortices increasing with increase in *Re*. The green isosurfaces also demonstrate the growth of the SPI mode at the stagnation point for $Re \geq 4000$. This mode might
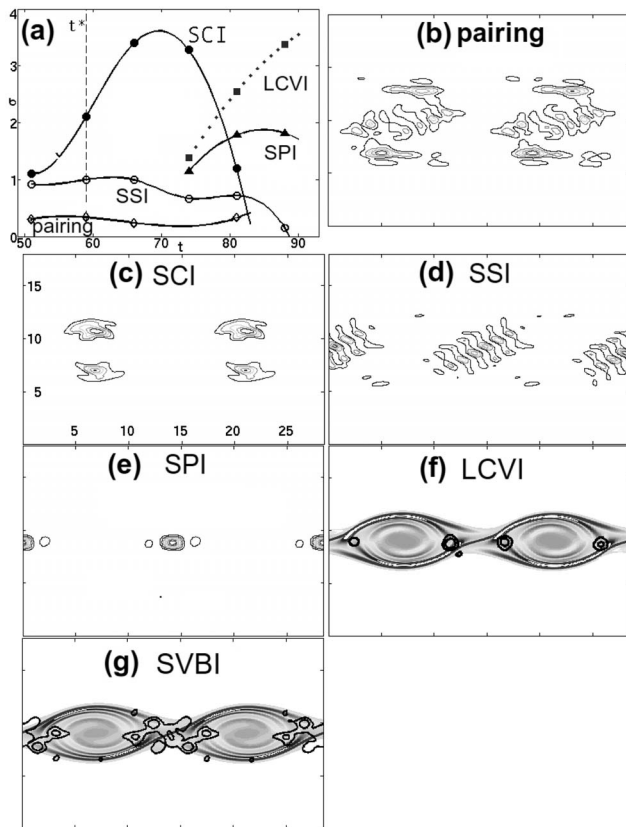
Figure 1. (a) Time evolution of growth rates of secondary instabilities for $Re = 2000$, $Ri = 0.12$, $Pr = 1$. Eigenfunctions are shown for (b) pairing instability, (c) Secondary Convective instability (SCI), (d) Secondary Shear Instability (SSI), (e) Stagnation Point Instability (SPI), (f) Localized Core Vortex Instability (LCVI) and (g) Secondary Vorticity Band Instability (SVBI).

be mistaken for SSI vortices at high Reynolds number (e.g., $Re = 8000$ in Figure 2) but it is important to note that they are fundamentally different. SPI is a localized phase-locked instability which remains stationary at the stagnation point
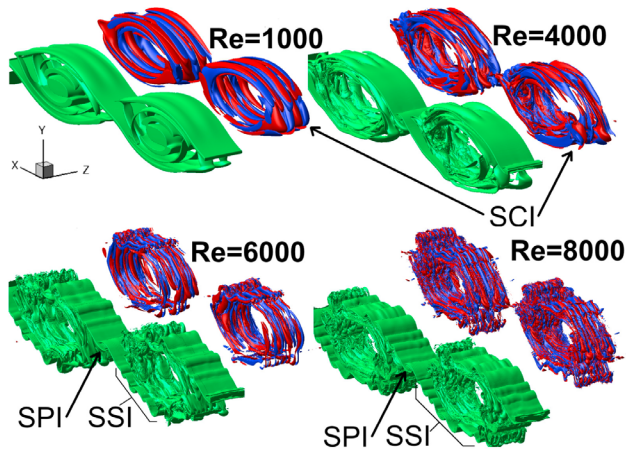

Figure 2. Spanwise vorticity iso-surfaces for $\omega_z = 0.72$ in green and streamwise vorticity iso-surfaces of $\omega_x = 0.2$ (red) and $\omega_x = -0.2$ (blue). $Ri = 0.12$ and $Pr = 1$ for all cases.

for considerable time whereas SSI vortices propagate along the braid and towards the cores upon their formation. Furthermore, SPI has a considerably larger spanwise wavenumber than SSI making it a more effective contributor to turbulent collapse. Figure 2 demonstrates that even though the braid instabilities do play a role in transition to turbulence, the SCI still emerges in the SARs forming counter-rotating shear-aligned vortices (shown with blue and red iso-surfaces in Figure 2) which wrap around the cores. Our analyses reveal that up to $Re \sim 10^4$ the breakup of these shear-aligned vortices remains the main contributor to a fast turbulent collapse of the billows. To demonstrate this, Figure 3 shows plots of the kinetic energy of the 3D instabilities ($\mathcal{K}_{3D}$) in Figure 3a along with contributions to growth of $\mathcal{K}_{3D}$ in Figure 3b for $Re = 1000$ (red lines) and $Re = 8000$ (black lines). Exact definitions of the quantities are given by CP00. The $\mathcal{K}_{3D}$ curves show rapid growth of 3D perturbation energy from a near-zero value to a saturation level due to emergence of various 3D instabilities. Figure 3b shows partial breakdown of the contributions to growth of $\mathcal{K}_{3D}$ during the time of rapid transition shown in Figure 3a ($40 < t < 110$). For both $Re = 1000$ and $Re = 8000$, 3D-buoyancy flux (solid lines) plays a dominant role in transition to 3D turbulence despite the large difference in Re. The peak in the buoyancy flux curve is a characteristic of the overturning of the unstable regions of the cores due to growth of the SCI. This confirms that the SCI remains the dominant player in the transition process as Re increases to values realized in nature. The dashed lines in Figure 3b show the extraction of 3D perturbation energy from the 2D KH billow through the action of shear. For $Re = 1000$, the peak ($65 < t < 85$) corresponds to the growth of the SVBI while for $Re = 8000$, the peak ($50 < t < 80$) is due to growth of
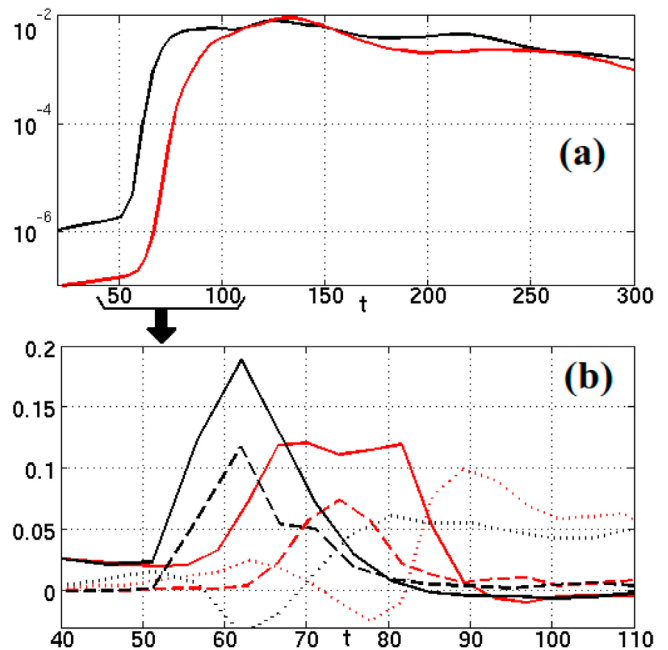

Figure 3. (a) Non-dimensional 3D perturbation kinetic energy (K_{3d}). (b) Contributions to growth of K_{3d} by 3D buoyancy flux (solid line), energy extraction from the 2D KH flow field (dashed line) and energy extraction from the mean background field (dotted line). Black and red lines correspond to $Re = 8000$ and $Re = 1000$, respectively.
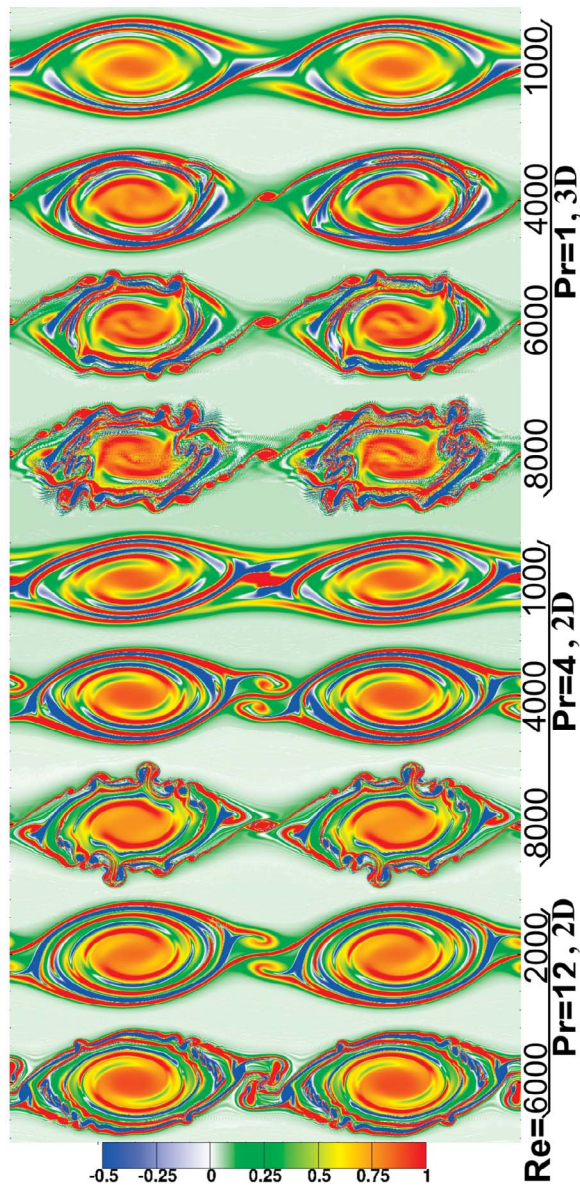
Figure 4. Spanwise vorticity (ω_z) contours on $X - Y$ plane for 3D simulations of Figure 2 along with 2D simulations for $Pr = 4, 12$.

SPI and SSI on the braid. It was shown in MP1 that braid instabilities extract most of their energy from the primary KH billow. The dotted lines in Figure 3b show the contribution to growth of $\mathcal{K}_{3D}$ through shear extraction from the mean background field. For both cases, once the flow becomes turbulent and the unstable regions inside the cores are eroded by reversible and irreversible motions, shear extraction from the background flow will be the dominant driving mechanism of 3D motions.

[11] Figure 4 shows side view vorticity plots of the simulations on the basis of which Figure 3 was produced along with results from 2D simulations performed for higher Prandtl numbers. Comparison between 2D simulations for $Pr = 1$ discussed in MP1 with 3D simulations for $Pr = 1$ shown in Figures 3 and 4 (in this paper) shows that 2D simulations provide insight into the order of emergence of secondary instabilities in the flow (excepting the 3D SCI)

and this justifies our use of 2D simulations in Figure 4 for higher Prandtl numbers, a decision required due to the restriction imposed by computational resources. Comparison between the cases for each Prandtl number in Figure 4 shows that increase in Re leads to emergence of secondary vortices on the braid as expected according to Figure 2. However, the abundance of secondary vortices formed on the braid diminishes as Prandtl number is increased which is in agreement with MP1 (see auxiliary material). This can be verified by comparing the $Re = 4000, 6000$ cases for $Pr = 1$ and $Pr = 4$. Figure 4 shows that SPI is promoted by increase in both Re and Pr. The influence of Pr on SPI is easier to observe since SPI does not onset at low Reynolds numbers (up to a few thousand; see MP1) for $Pr = 1$ while at higher Pr, it emerges at Re as low as 1000.

[12] The finite amplitude growth of the SPI is also greatly influenced by Pr because SPI arises due to interaction between vorticity layers at the periphery of the cores and the braid. At higher Prandtl numbers, these vorticity bands retain sharp gradients due to smaller diffusivity (assuming that Re is kept constant) and so the interactions between the cores and the braid become stronger leading to larger deformations at the stagnation point as shown in Figure 4 for $Pr = 4$ and 12. The core deformation due to SPI also becomes more significant for these cases and the instability looks to be more of SVBI type. It should be noted that increase in Pr also promotes the SCI and in 3D reality, it is quite possible that early and rapid growth of SCI would inhibit large amplitude growth of SPI such as that shown in Figure 4 for $Pr > 1$. The evolution of the SPI (or SVBI) is also greatly influenced by that of the SSI. At each fixed Prandtl number, as Re increases, the SSI vortices form earlier in the evolution of the KH wave and in greater number and therefore modify the evolution of the SPI through the deformation they cause in the braid and in the cores (e.g., compare $Re = 4000$ and $Re = 8000$ cases for $Pr = 4$). Therefore, at each Pr, there will be a range of intermediate Reynolds number in which the SPI-SVBI instability can grow significantly, and above which the SSI vortices will form in abundance thereby influencing (and maybe prohibiting) the evolution of SPI-SVBI (such as results of G10), and below which SPI and SSI will not fully emerge. Even though finite amplitude growth of SPI-SVBI has not been reported in either laboratory measurements (due to low Re) or observational data (due to low resolution of the images), we suggest that evidence of this instability might already exist in observational studies such as *Geyer et al.* [2010, Figure 4], *Moum et al.* [2003, Figure 14] and perhaps *Bourgault et al.* [2001, Figure 5c]. This issue will require further investigation.

[13] Numerous observational studies of mixing in shear zones such as estuaries reveal well mixed regions within the cores of the KH waves with noticeably larger dissipation in the braid region and in the periphery of the cores [*Geyer et al.*, 2010; *Tedford et al.*, 2009]. Two important points need to be made regarding the interpretation of such observations: First, there is not a clear separation between the braid and the cores and the braid usually connects to the corners of the outermost SARs inside the cores. Second, observations of well-mixed regions inside the cores at early stages of flow evolution still require explanation. As for the first point, it is quite possible that the dissipation regions referred to as braids in the observational studies also include

the SARs which have gone convectively unstable. A comparison between the eigenfunctions of the SCI shown in Figure 1 (for $Re = 2000$) and in MP1, CP00, and KP85 for $Re = 1000, 750, 300$, respectively, shows that with increase in the Reynolds number, the shear-aligned convective rolls formed due to growth of the SCI tend to emerge earlier in flow evolution and to wrap more closely around the cores (see Figure 3). Figures S1c and S1d in the auxiliary material show side views of the high-Re simulation of Figure 3 and demonstrates how the tips of the braid are blended into the SARs right before the SARs become convectively unstable. At high Re, SSI vortices evolve early in the evolution of a KH wave and before SCI grows. Therefore, observational images of KH wave trains are sometimes captured before the emergence of SCI (which leads to fast turbulent collapse of the billows). As for the second point concerning the well mixed regions inside the cores in the observed KH waves, the core interiors are known to be highly-diffuse regions (CP00). Moreover, at high Reynolds numbers, small scale disturbances which grow on the braid travel towards the cores leading to enhanced diffusion in the cores' periphery by deforming the core vorticity bands and also by excitation of new instabilities in the periphery of the cores. Both of these effects are shown in high Re cases of Figure 4 (and also in Figure S1a in the auxiliary material). Rayleigh-Taylor type instability can be clearly observed at the top and bottom of the core consistent with previous experimental results [*Atsavapranee and Gharib*, 1996]. Moreover, at higher Pr, the vorticity layers inside the cores retain sharp gradients for a longer time and become susceptible to a range of small scale secondary instabilities such as those shown in high Re and $Pr > 1$ cases of Figure 4 (and also in Figures S1a and S1b in the auxiliary material. Of particular interest is the secondary shear instability of the core's interior vorticity bands shown in the last frame of Figure 4 (and also in Figure S1b). These secondary core instabilities along with the possibility of emergence of SCI at early stages of evolution of the primary KH billow (at high Re) may explain the absence of observations of the "spaghetti roll" configuration (which is typically observed inside the cores of KH billows in numerical experiments) in geophysical flows such as those discussed by G10.

[14] Finally, it should be mentioned that the stratification level has a great influence on the probability of occurrence of various secondary instabilities (as discussed in connection with Figure 2). As discussed by MP1 for $Pr = 1$, this influence differs from one instability to another.

[16] The Editor thanks the two anonymous reviewers for their assistance in evaluating this paper.

References

Atsavapranee, P., and M. Gharib (1997), Structures in stratified plane mixing layers and the effects of cross-shear, *J. Fluid Mech.*, *342*, 53–86.

Bourgault, D., F. J. Saucier, and C. A. Lin (2001), Shear instability in the St. Lawrence Estuary, Canada: A comparison of fine-scale observations and estuarine circulation model results, *J. Geophys. Res.*, *106*, 9393–9409.

Caulfield, C. P., and W. R. Peltier (2000), Anatomy of the mixing transition in homogeneous and stratified free shear layers, *J. Fluid Mech.*, *413*, 1–47.

Corcos, G., and F. Sherman (1976), Vorticity concentration and the dynamics of unstable free shear layers, *J. Fluid Mech.*, *73*, 241–264.

Geyer, W. R., A. C. Lavery, M. E. Scully, and J. H. Trowbridge (2010), Mixing by shear instability at high Reynolds number, *Geophys. Res. Lett.*, *37*, L22607, doi:10.1029/2010GL045272.

Gossard, E. E. (1990), Radar research on the atmospheric boundary layers, in *Radar in Meteorology*, edited by D. Atlas, chap. 27a, p. 477–527, Am. Meteorol. Soc., Boston, Mass.

Klaassen, G. P., and W. R. Peltier (1989), The onset of turbulence in finite amplitude Kelvin-Helmholtz billows, *J. Fluid Mech.*, *155*, 1–35.

Luce, H., T. Mega, M. K. Yamamoto, M. Yamamoto, H. Hashiguchi, S. Fukao, N. Nishi, T. Tajiri, and M. Nakazato (2010), Observations of Kelvin-Helmholtz instability at a cloud base with the middle and upper atmosphere (MU) and weather radars, *J. Geophys. Res.*, *115*, D19116, doi:10.1029/2009JD013519.

Mashayek, A., and W. R. Peltier (2011), The "zoo" of secondary instabilities precursory to stratified shear flow transition. Part I: Shear aligned convection, pairing, and braid instabilities, *J. Fluid Mech.*, in press.

Moum, J. N., D. M. Farmer, W. D. Smith, L. Armi, and S. Vagle (2003), Structure and generation of turbulence at interfaces strained by internal solitary waves propagating shoreward over the continental shelf, *J. Phys. Oceanogr.*, *33*, 2093–2112.

Peltier, W. R., and C. P. Caulfield (2003), Mixing efficiency in stratified shear flows, *Annu. Rev. Fluid Mech.*, *35*, 135–167.

Staquet, C. (1995), Two-dimensional secondary instabilities in a strongly stratified shear layer, *J. Fluid Mech.*, *296*, 73–126.

Staquet, C. (2000), Mixing in a stably stratified shear layer: Two-and three-dimensional numerical experiments, *J. Fluid Mech.*, *27*, 367–404.

Smyth, W. D. (2004), Secondary Kelvin-Helmholtz instability in weakly stratified shear flow, *J. Fluid Mech.*, *497*, 67–98.

Tedford, E. W., J. R. Carpenter, R. Pawlowicz, R. Pieters, and G. A. Lawrence (2009), Observation and analysis of shear instability in the Fraser River estuary, *J. Geophys. Res.*, *114*, C11006, doi:10.1029/2009JC005313.

Thorpe, S. A. (2005), *The Turbulent Ocean*, Cambridge Univ. Press., Cambridge, U. K.

van Haren, H., and L. Gostiaux (2010), A deep-ocean Kelvin-Helmholtz billow train, *Geophys. Res. Lett.*, *37*, L03605, doi:10.1029/2009GL041890.

A. Mashayek and W. R. Peltier, Department of Physics, University of Toronto, 60 St. George St., Room 609, Toronto, ON M5S 1A7, Canada. (amashaye@atmosp.physics.utoronto.ca)